

Artículo aceptado en / *Paper accepted in*

REVISTA MEXICANA DE CIENCIAS GEOLÓGICAS



Versión preliminar / *Draft versión*

Determination of the effective storage of CO₂ at Coyula seismic block level in the Tampico-Misantla province

por / *by*

Erik Medina, Gilles Levesse, Cesar A. Cortes-Prado, Mariano Cerca, Jaime Carrera-Hernandez, and Berengere Mougel

© 2026 The authors

<https://creativecommons.org/licenses/by/4.0/>



Manuscript received: August 6, 2025
Corrected manuscript received: March 31, 2025
Manuscript accepted: April 6, 2026
Draft version published: April 27, 2026

Determination of the effective storage of CO₂ at Coyula seismic block level in the Tampico-Misantla province

Erik Medina¹, Gilles Levresse², Cesar A. Cortes-Prado¹, Mariano Cerca²,
Jaime Carrera-Hernandez², Berengere Mougel²

¹ Posgrado en Ciencias de la Tierra, Universidad Nacional Autónoma de México, Campus Juriquilla Blvd. Juriquilla 3001, Querétaro, 76230, México

² Instituto de Geociencias, Universidad Nacional Autónoma de México, UNAM Campus Juriquilla Blvd. Juriquilla 3001, Querétaro 76230, México.

**Corresponding author (G. Levresse): glevresse@geociencias.unam.mx*

ABSTRACT

Carbon Capture and Storage (CCS) is commonly accepted as an essential mitigation of atmospheric CO₂ concentrations. Despite being a significant petroleum producer, Mexico is committed to combating climate change encouraging the use of CCS and EOR technology. The storage capacity of CO₂ in the deep saline aquifer's reservoir located in the Coyula seismic block in the Tampico Misantla Basin is estimated using the volumetric approach where parameters like CO₂ density, and porosity of the geological formation, and efficiency storage factor are considered. To achieve a better evaluation of the site and to constrain the effective storage potential of the Coyula seismic block, both open and close systems were tested. A conservative evaluation for the three reservoirs delimited in the Cahuadas Jurassic formation within the Coyula seismic block amounts to 25.6 Mton CO₂. Compared to the emissions from regional sources (8 Mton of CO₂ per year), the minimum geological reservoir evaluation encourages further detailed studies to improve the estimation of reservoir volumes and CO₂ storage feasibility.

Keywords: Screening and evaluation of CO₂ storage; Saline aquifer; CO₂ storage; regional characterization

INTRODUCTION

The increasing concentration of CO₂ in the atmosphere due to the development of industrial activity during the last century has significantly impacted the global climate, the ecological environment and is currently jeopardizing our way of life.

Concerned for the consequences of carbon concentrations, societies have called for a global effort to limit the CO₂ emissions or to reverse the increasing trend of CO₂ concentration in our atmosphere. To reduce the amount of CO₂ in the atmosphere, Carbon Capture and Storage (CCS) has been recommended as a viable option (Torp and Gale, 2003).

Accordingly, CCS methods have been continuously developed since the 1990s. One of the most promising approaches is CO₂ storage in saline aquifers, because they offer an high-potential carbon storage potential under CO₂ supercritical conditions (31.1°C and 7.38 MPa), and CO₂ can be retained at depth through several processes, such as structural/stratigraphic trapping, residual trapping (capillarity force in porosity at irreducible gas saturation), solubility trapping (dissolved into formation water), as well as mineral trapping (incorporated in newly formed minerals during water/rock interaction). As any geological injection processes, injection of CO₂ into deep saline aquifers is not an easy task. It requires a multicomponent, multiphase flow system, in which geomechanics, geochemistry, and thermal effects may be important (Al-Khoury and Bundschuh, 2014).

The capacity of CO₂ storage in geological formation is not consequently a straightforward or simple process. Luo et al. (2022) have recently reviewed the different storage mechanism applied worldwide and pointed out the challenges of the different stage's evaluation involved. The CO₂ storage capacity estimation methods are divided in static and dynamic methodologies. Static methods of estimating CO₂ capacity involve analyzing the physical properties of the aquifer, such as porosity and permeability, to calculate the total volume. The dynamic methods involve simulating the fluid flow and transport processes in the aquifer to estimate the effective storage potential, and the CO₂ behavior over the time (Bachu, 2007). The dynamic methods require defining more data to characterize the thermal mechanic and hydrologic processes. It also requires more precise boundary conditions of the potential reservoir rock and fluids. In close systems, the reservoir volume is restricted by the impermeable geological boundary (structural or stratigraphic), which prevent fluid movement, and volume variation. Conversely, open systems permit vertical

and/or lateral fluid movements through permeable boundaries, thereby increasing porosity availability and enabling volume variations.

This study evaluates the CO₂ storage potential of Jurassic saline aquifers in the Tampico-Misantla Basin, focusing on Coyula seismic block scale as a last step before dynamic, site-specific evaluations. The main objective is to estimate effective storage capacity using locally derived petrophysical data, aiming to reduce uncertainty associated with global averages commonly used in previous studies, such as those by the IEA-GHG (2009). A lithostratigraphic-structural model was developed, identifying three potential storage sites within the basin. Static storage capacity was calculated using effective storage coefficients tailored to local geological conditions. This approach addresses challenges related to limited site-specific data, which currently prevent detailed dynamic modeling of CO₂ flow and transport. The study builds on prior regional assessments that highlighted the basin's suitability for carbon capture and storage (CCS), offering refined estimates that can support future CCS planning and implementation in northeastern Mexico.

GEOLOGICAL FRAMEWORK

The central part of the Mexican continental margin of the Gulf of Mexico is composed of the Tampico Misantla basin (TMB) (Figure 1) which consists of a low-lying (0 to 500 m.a.s.l) mountainous plain. Its northern part is bordered by the Sierra de Tamaulipas, and to the south is the Trans Mexican Volcanic Belt. On the western and eastern sides, the TMB is bounded by the Gulf of Mexico, and the Sierra Madre Oriental, respectively

The Sierra Madre Oriental belongs to the Mexican Fold and Thrust Belt tectonic unit (MFTB; Figure 1) (Fitz-Díaz et al., 2018). Its formation is related to the Laramide Orogeny and the associated subsidence of former carbonate platforms together with the development of Late Cretaceous–Paleogene flexural Mexican foreland basins (MFB, Figure 1; Laville et al., 2004; Suter, 1980; Roure et al., 2009; Lawton et al., 2016) including the Burgos (BB), the Tampico-Misantla (TMB), and the Veracruz basin (VB). The MFB forms a large and low-altitude terrain in direct contact with the MFTB (Eguiluz de-Antuñano, 2011; Nieto-Samaniego et al., 2013). Overall, the TMB itself exhibits a complex geological record, where Mesozoic sediments overlie

the Precambrian and Paleozoic basement, which in turn underlies Triassic units of volcanic and sedimentary origin (Carrillo-Bravo, 1971; Fitz-Díaz et al., 2018).

Figure 1 presents a geological map detailing the lithology of geological units from the region, as well as the main structures which show evidence for tectonic shortening and extension. The sedimentary and structural contacts between units from the Jurassic to more recent periods are illustrated in a redrawn regional geological cross-section from the Comisión Nacional de Hidrocarburos (2018) (A-A' profile in Figure 1). It is worth pointing out that the study area has been affected by the pre- and syn- rifting and drifting episodes of the Gulf of Mexico (GOM) during the Jurassic (Coombs et al., 2020), which led to the reworking of the continental rocks and syn-rift sediments formed before the Jurassic (Amaral et al., 2021). The subsequent rotational opening of the GOM coupled with the Yucatan Block's translation enabled the formation of north-south regional shear zones across eastern Mexico (Pindell et al., 2020; Coombs et al., 2020). These zones accommodated substantial displacements, fragmenting paleogeographic elements like the massif of Chiapas and that of Tampico (Pindell et al., 2020; Coombs et al., 2020) and ultimately followed by the development of the extensional TMB (Martini and Ortega, 2018). Reported evidence for post-rift facies and carbonate platform deposition (Hernández-Romano et al., 1997) suggest that a passive margin environment was prevailing throughout much of the Cretaceous. However, during the Paleocene-Eocene, the deformation characterized by significant shortening led to the formation of the Chicontepec foreland sub-Basin, being related to the Mexican Orogenic event (Fitz-Díaz et al., 2018). This basin is composed of siliciclastic sediments deposited during the orogenic period (Eguiluz de Antuñano et al., 2011; Fitz-Díaz et al., 2018). Consequently, formations formed prior and during the Mesozoic experienced deformation and structuring within the fold-thrust belt (Dávila et al., 2010), with the migration of the shortening front towards the east and overriding units of Middle Cretaceous age onto sedimentary deposits from the Eocene (Figure 1). The oldest formations found within the TMB are represented by the Huayacocotla and Cahuadas Formations, dating back to the Toarcian and Callovian ages, respectively (Figure 1). The Huayacocotla Formation, is mainly composed of quartz-rich conglomerates and sandstones, originated in a continental basin (Esquivel-Macías et al., 2017). In contrast, the Cahuadas Formation is composed of conglomerates, sandstones, siltstones, and shales reflecting a fluvial and alluvial depositional environment (López-Infanzón, 1986). This continental phase ended-up with the deposition during the Middle Jurassic of, wackestone, anhydrite mudstone, and anhydrite,

composing the Huehuetepec Formation (Nava-Pérez & Alegría-Luna, 2001). Subsequently, the Upper Jurassic units known as the Pimienta, Tamán, and Tepexic-Santiago formations show radical changes in composition with the presence of limestones, carbonaceous mudstones, and shales rich in organic matter. Concurrently, oolitic limestones, likely deposited at the basin margin, can be found in the San Andrés Formation (Todd, 1976). Predominant Sedimentary facies recorded during the Cretaceous are that of basin and oceanic shelf, with carbonate reefs developing on paleogeographic summits (López-Doncel, 2003; Rodríguez-Hernández, 2007). This entire period is characterized by gentle and prolonged subsidence. The lower part of the Tamaulipas Formation marks a transition phase during the Early Cretaceous, beginning with grainstones (oyster shape) and packstones interspersed with layers composed of bentonite and shale, and gradually transitioning to thicker limestone units upward (Hernández-Romano et al., 2006). Maximum estimated subsidence depth occurred during the Albian-Cenomanian, with oceanic basin deposition facies. The upper part of the Tamaulipas Formation comprises limestones and shales of argillaceous and calcareous compositions, respectively. Early Cretaceous is represented by Santuario, Tamabra, El Abra, and Tamaulipas calcareous and carbonaceous formations. While the Santuario Formation mainly consists of limestones (dark-gray color), calcarenites, greywackes, and phyllitic shales (Segerstrom, 1962), the other formations are primarily composed of limestones. Notably, the Tamabra Formation includes interbedded calcareous breccia, the el Abra Formation features thick-bedded limestone, and the Tamaulipas Formation exhibits limestones with chert lenses and some evaporites at its bottom (Guaxcama Fm.). The Agua Nueva Formation (Early Turonian) is characterized by limestones enriched in clay and carbonates as well as calcareous shales. Formations known as San Felipe and Méndez are also very similar to Agua Nueva although they exhibit bentonite intercalations (Seibertz, 1986). During the Paleogene, the dominant sedimentary facies became siliciclastic, comprising a thick sequence of landslides, debris flows, and turbiditic flows that filled foreland basin of the Sierra Madre Oriental. These units are called Velasco, Chicontepec, and Guayabal formations (after Barker and Berggren, 1977). This period is also represented by the formation of the Bejuco-La Laja paleo-canyon and the Chicontepec paleo-channel (Santillán-Piña & Aguayo-Camargo, 2011). The upper portion of the overall detritic sequence, spanning from the Oligocene to the Recent, is composed of interbedded sandstones and shales, illustrated by Tantoyuca, Chapopote, Horcones, Palma Real, Mesón, and Tuxpan formations (Guzmán-Arellano, 2012).

The sedimentary column of the TMB also shows some magmatic intrusions of Middle Eocene to Quaternary ages associated with the Eastern Mexican Alkaline Province (EMAP). In the northern part of the TMB, as well as in Tamaulipas highs, these intrusions primarily consist in porphyritic and equigranular bodies, with minor hypabyssal igneous bodies, dating between approximately 44 and 20 million years ago (Hamblock, 2002; Poliquin, 2009; Viera-Décida et al., 2009). Later (< 16 million years ago) prevalent lava flows and dikes have been reported within the basin (Ferrari et al., 2005). East of the TMB lies the Aldama Volcanic Field, composed of alkali basalts and derived olivine trachytes from the Pliocene to the Pleistocene exhibiting geochemical signatures typical of intraplate magmatism (Camacho-Angulo, 1993; Aranda-Gómez et al., 2005). Finally, the Llera de Canales Volcanic Field, located west of the Sierra de Tamaulipas and contemporaneous with the Aldama Volcanic Field, reports some basanitic lava flows, some alkaline basalts, and sodic trachybasalts (i.e. hawaiites) lava flows (Aranda-Gómez et al., 2005 and references therein). Viera-Décida et al. (2009) also suggested that the igneous rocks from Palma Sola and from Los Tuxtlas that have been emplaced during the Late Upper Oligocene to Miocene, at the southern border of the TMB, may represent the southernmost extent of the EMAP.

RESERVOIR CHARACTERIZATION

Comisión Nacional de Hidrocarburos (CNH) data from oil wells penetrating the Jurassic column were used to characterize the petrophysical properties of the target saline aquifers. Regional 3D seismic reflection surveys are combined with detailed well-log analyses from Pemex-PEP exploration wells. Lithology mudlogs, which describe the main rock types within specific depth intervals, are constructed using core descriptions. These descriptions encompass key features such as grain size, mineralogy, grain distribution, matrix composition, density, and fluid content.

Wells selection

Five wells—Planos-1, Palmar-1, Tablon-1, Defense-1, and Tecomate-1—met the primary selection criteria: availability of geological and petrophysical data, and penetration into the Jurassic sedimentary sequence within the seismic survey area (Figures 2 and 3). These wells encountered the reservoir Jurassic formations at depths ranging from 3200 to 4900 meters below

the surface. Penetration depth into the Jurassic formations varied among the wells. All five wells intersected the uppermost 500 to 600 meters of the Jurassic column. The Cahuwasas Formation, characterized by sandstone lithology, constitutes the top of the Jurassic sequence. This formation maintains a relatively consistent thickness of approximately 400 meters across the Coyula 3D seismic block. Overlying the Cahuwasas sandstone is the Huehuetepc Formation, composed of Upper Jurassic shale. Notably, the base of the Huehuetepc Formation contains discontinuous evaporite layers. These evaporite layers serve as both a reliable marker horizon for stratigraphic and petrophysical correlation and an effective caprock due to their distinct geological and petrophysical properties.

The seismic model and reservoir volume estimation

A lithostratigraphic-structural model of the study area was constructed using Petrel® software (version 2013). The 3D seismic reflection cube was calibrated using data from the five positioned well logs. Regional interpretation of the seismic data, with a 25-meter profile spacing, identified key stratigraphic horizons and faults. Following digitization and interpretation (2D), the faults and stratigraphic tops were converted into surfaces, forming the basis of the 3D stratigraphic-structural model. Linear interpolation was employed for this conversion. To estimate reservoir volume, a 3D geocellular model was built using the interpreted structural and stratigraphic data from the depth-converted 3D seismic cube. Geological contacts defined using well log data, lithological descriptions, and paleontological reports, guided the interpretation of surfaces and faults. This interpretation informed the creation of a structural model with sub-horizons and faults, which was then used to generate a 3D orthogonal cell grid comprising 225,600 cells and 237,456 nodes. Petrophysical properties, including porosity and permeability, were extrapolated through the 3D cell grid using geostatistical methods constrained by interval velocity and validated with core measurements. Finally, a geometric volume was calculated for each cell, and an index filter was applied to delineate the prospective reservoirs

Petrophysical properties

Porosity and permeability

Porosity and permeability were initially determined from well-log measurements and then validated against core sample analyses from Tecomate-1 well to ensure accurate representation of these well-log reservoir properties. Two methods, Wyllie Time Average (sonic porosity) and Neutron porosity, were employed to estimate porosity. Permeability was determined using the Wyllie-Rose method for sands and the Coates and Dumanoir method for fine-grained facies. Notably, the sonic porosity and Wyllie-Rose permeability estimations demonstrated good agreement with helium porosity and steady-state permeability measurements conducted on core samples from the Tecomate-1 well. These core samples, extracted from calcareous sandstone facies at the top of the Cahuwasas Formation, provided valuable ground truth data. Furthermore, a lithological index, integrating porosity and permeability information, was interpreted to classify the predominant facies within the Tamán, Tepexic, Santiago, and Cahuwasas formations, enhancing the understanding of reservoir heterogeneity.

Vertical stress and pore pressure profiles

The vertical stress profile was determined using a combination of bulk density logs and extrapolated density estimations for shallow intervals where log data might be limited. Vertical pore pressure profiles were estimated using the Eaton method, which utilizes compressional slowness logs (Eaton, 1972). These estimations were then validated against mud density profiles and gas reports for accuracy. Mud-loss pressure profiles were estimated using the Matthews and Kelly (1972) method, assuming a ratio of 0.75 between the vertical stress and the minor horizontal stress. This assumption is often used in regions with limited stress data. These estimations were further validated against mud-loss and ballooning events documented in drilling reports from five offset wells, providing valuable insights into actual wellbore conditions. The use of offset well data enhances the reliability of the mud-loss pressure profile.

Dynamic elastic modulus

The dynamic elastic modulus was determined using density and sonic log data (compressional and shear). Where density log data were unavailable, a correlation between compressional sonic and density logs, tailored to the specific lithological facies, was employed.

The shear sonic log, a key component in calculating the dynamic elastic modulus, was estimated using Castagna (1985) relations for saturated sandstones and shales. This approach leverages the relationship between compressional and shear wave velocities in different lithologies. It is important to note that the dynamic elastic modulus, estimated from acoustic wave propagation in an isotropic elastic medium, is typically higher than the static elastic modulus. This difference arises because dynamic measurements, acquired under dynamic conditions, involve smaller deformation amplitudes compared to static measurements.

Effective storage capacity estimation

Structural highs, representing structural traps, were identified as potential CO₂ storage sites. This selection was based on the positive buoyancy of CO₂, which tends to migrate upwards, and the presence of coarse-grained alluvial fan deposits (sandstones) within these structures, providing suitable reservoir characteristics. However, due to limited data on the hydraulic properties (specifically, transmissivity) of the faults bounding these potential reservoirs, two boundary condition scenarios were considered, open and closed systems. A closed system assumes that faults behave as sealing boundaries, effectively compartmentalizing the reservoir and restricting fluid flow to the defined structural closure. In contrast, an open system allows for hydraulic connectivity with adjacent stratigraphic or structural units, enabling pressure dissipation and fluid exchange across boundaries. Evaluation of these end-member scenarios constrains the envelope of possible system behaviors and supports a more rigorous quantification of volumetric capacity and dynamic uncertainty. The closed system represents the most conservative, capacity-limited scenario.

Open system

To estimate the effective storage capacity of the identified geological structures as open systems, we employed the DOE methodology with a probabilistic approach. This approach utilizes effectiveness coefficients representing the P10, P50, and P90 percentiles for parameters influencing storage capacity (DOE, 2009). The total CO₂ storage capacity (GCO₂T) is calculated using the following equation:

$$G_{CO_2T} = A \times h \times \Phi \times \rho_{CO_2} \times E_E \quad \text{Eq. 1}$$

where:

A: Reservoir area (give in m^2 , obtained from seismic and petrophysical data (Figure 6))

h: Reservoir thickness (give in m, obtained from seismic and petrophysical data (Figure 6))

Φ : Porosity (give in m^3/m^3 , calculated from well logs and laboratory analyses (Figure 6))

ρ_{CO_2} : CO_2 density (give in kg/m^3 , estimated based on reservoir depth and temperature)

E_E : Efficiency coefficient (calculated using Eq. 2)

To estimate realistic values for the storage capacity of the specific stratigraphic units (A, B, C), we decide to use the most conservative characteristic values for the different horizon in the considered properties.

The efficiency coefficient (E_E) represents the combined effect of geological, volumetric, and microscopic displacement efficiencies (IEA-GHG, 2009):

$$E_E = E_{Geol} \times E_V \times E_d \quad \text{Eq. 2}$$

E_{Geol} is the geological efficiency (dimensionless). This factor accounts for the portion of the geological unit suitable for CO_2 storage, considering net area, net thickness, and effective porosity:

$$E_{Geol} = (A_n/A_t) \times (h_n/h_g) * (\Phi_{ef}/\Phi_T) \quad \text{Eq. 3}$$

where:

A_n (Net area): expressed in square meters (m^2).

A_t (Total area): expressed in square meters (m^2).

A_n/A_t : Net-to-gross area ratio (dimensionless), determined from petrophysical models using a minimum total porosity cut-off of $\phi_{tot} = 0.10$.; (Hatzignatiou et al., 2011)

h_n/h_g : Net-to-gross thickness ratio (dimensionless), derived from well logs using a clay volume cut-off of 0.20; thickness values are expressed in meters (m). (Figure 4))

- ϕ_{ef} (Effective porosity): expressed as a fraction or percentage (v/v). It represents the interconnected pore space available for fluid flow and storage (dimensionless).

- ϕ_t (**Total porosity**): expressed as a fraction or percentage (v/v). It includes both connected and isolated pores, as well as bound water associated with clays (**dimensionless**).

- Φ_{ef}/Φ_T : Effective porosity fraction. (calculated from petrophysical logs, (Figure 3).) dimensionless (fraction), indicating the proportion of the total pore space that effectively contributes to fluid flow or storage.

E_v (volumetric displacement efficiency) represents the fraction of pore space accessible to CO₂ injection. Due to limited data on reservoir heterogeneity, E_v values were derived from the IEA report (Appendix E corresponding to sandstones of an alluvial fan depositional environment).

E_d (efficiency of microscopic displacement) represents the fraction of pore space where CO₂ can effectively displace the existing fluids (e.g., water). It is calculated using the following equation (Bassiouni, 1994):

$$E_d = 1 - S_{wirr}$$

$$\text{where } S_{wirr} = \sqrt[n]{\frac{aRw}{\Phi_T^m R_t^2}}$$
Eq. 4

where:

S_{wirr} : Irreducible water saturation (the fraction of pore space occupied by immobile water, dimensionless)

R_w : Water resistivity (given in Ohmmeter, obtained from well logs)

Φ_T : Total porosity (obtained from well logs, dimensionless)

R_T : Deep penetration resistivity (given in Ohmmeter, obtained from well logs)

a, m, n : Empirical constants (dimensionless)

For this study, the following values were used based on the lithology (Carbonate rocks: $a = 1, m = 2$; Silicoclastic rocks: $a = 0.62, m = 2.15$, (Table 1; Archie, 1942).

These parameters, along with the well log data, allow for the calculation of E_d , which contributes to the overall efficiency coefficient for estimating CO₂ storage capacity.

Close systems

For closed systems, where CO₂ migration is restricted, the storage capacity calculation considers the compressibility of the rock and fluids. The equation for total CO₂ storage capacity in a closed system is:

$$G_{CO_2T} = A \times h \times \Phi \times \rho_{CO_2} \times E_{comp} \quad \text{Eq. 5}$$

where:

E_{comp} : Compressibility effectiveness coefficient (given in Mpa, calculated using Eq. 6)

This coefficient accounts for the volumetric changes due to the compressibility of rock and water under increased pressure from CO₂ injection. It is calculated as follows (Zhou et al., 2008; DOE):

$$E_{comp} = (\beta_r + \beta_a)\Delta p \quad \text{Eq. 6}$$

where:

β_r : Rock compressibility (calculated as $1/K$, where K is the compressibility modulus obtained from the petrophysical model)

β_a : Water compressibility (assumed constant at $4.6 \times 10^{-10} \text{ Pa}^{-1}$)

Δp : Pressure increase, calculated as, where P_p is pore pressure, P_f is the pressure of fracturation (using the synthetic curves of effective porosity and DTCO measurements for each horizon of interest in the reservoirs (Eaton, 1975; Bowers 1995)).

The rock compressibility is determined by the relationship $\beta_r = 1/K$. The compressibility modulus K was obtained in each of the horizons of interest from the petrophysics model (Zimmerman, 1991; Ahmed, 2006; Table 1). The water compressibility (β_a) is considered a constant ($4.6 \times 10^{-10} \text{ Pa}^{-1}$; EIA-GHG, 2009).

DETERMINATION OF EFFECTIVE STORAGE CAPACITY IN SELECTED AREA

The CO₂ storage capacity for the Cahuasas Upper Jurassic formation within the Coyula seismic block was calculated based on the lithology and the petrophysical properties of the five

exploratory oil wells crossing the seismic block. Three main reservoirs were identified (A, B, C; Figure 5). All the reservoirs are sealed by a thick efficient caprock composed of shale and evaporite characterized for their very low permeability (Figure 4). The trapping mechanism involves stratigraphic trapping through lateral delta and alluvial fan facies variations. Figures 5 and 6 show the reservoirs A, B, C depth range from 3600 to 3900 m. The three reservoirs present the same lithology made off sandstone with shaly layers intercalation. For Accuracy, the CO₂ density is estimated as a density range, following the reservoir depth and thickness and reservoir temperature variation (Medina et al., 2023). The full data set use to develop the Eq. 1 for open system and Eq. 5 for close system are summarized in Table 1. We estimated the CO₂ potential storage resources for each Cahuascal stratigraphic layers of the three reservoirs (A, B, C). The range of the petrophysics characteristics are comparable in all reservoirs. The pore and fracture pressures vary from 36.9 to 46.5 MPa and from 72.8 to 90.8 MPa respectively. The reservoir A shows wider porosity and relative homogeneous permeability varying from 0.07 to 0.2 % and 0.26 to 2.5 mD, compared to B and C reservoirs, ranging from 0.12 to 0.18 % and from 0.2 to 6.5 mD. Irreducible water values varied between 47 to 60 %. The density of CO₂ is estimated as a min and max range from 417 to 663 kg/m³, considering the reservoir temperature and lithologic pressure. The reservoir volumes are underestimated and still comparable (Table 2). The volumes of Reservoirs A and B are constrained by the lateral extent of the seismic blocks rather than by stratigraphic closure (Figure 5).

For the determination of the effective storage coefficients in a closed system hypothesis, the porosity is presented as a weighted mean by reservoirs. The efficiency coefficient (E_E) estimate for each reservoir is comparable ranging from 1.79 (Res. C) to 2.03 (Res. A). The effective storage capacities of CO₂ are estimated as a min and max range. The results are presented in volumetric and mass effective storage capacity. The ranges vary from 3.83 to 6.09 Mton for reservoir A, from 4.93 to 7.83 Mton for reservoir B, and from 7.63 to 11.70 Mton for reservoir C, for a total at the Coyula seismic block ranging from 16.11 to 25.62 Mton CO₂. The most impacting data in the final CO₂ mass estimation is the reservoir volume.

For the open system hypothesis, we used the same petrophysical data than previously. We estimate efficient coefficients for open system for a sedimentary environment of sandstone deposited in an alluvial fan with a monoclinical structure, shown in the Table 4 for the 10, 50, and 90 percentiles (Table 1 and 4).

The results are presented in volumetric and mass effective storage capacity. Geological and petrophysical data vary in comparable way in the three reservoirs. Reservoir volume and the associated percentiles represent the key parameters that exert the greatest influence on the final storage potential estimation (Table 4). The maximum and minimum effective storage capacity obtained for the reservoirs in the Coyula block range from 11.21 to 17.28 Mton (P10) to 27.32 to 43.44 Mton (P90) for reservoir A, from 3.8 to 6.16 Mton (P10) to 9.69 to 15.41 Mton (P90) for reservoir B, and from 10.56 to 16.79 Mton (P10) to 38.35 to 60.97 Mton (P90) for reservoir C, for a total estimation at Coyula block of 25.65 to 40.78 Mton (P10) to 75.36 to 119.82 Mton (P90). We consider these values a conservative estimate for the potential of the Cahuasas sandstone.

When compared with capacity estimates from some of the most extensively studied CO₂ storage projects worldwide—such as Quest and Weyburn in Canada, Cranfield in the USA, Sleipner in Norway, and Gorgon and Otway in Australia—the results obtained in this study appear both consistent and promising. These reference sites span a range of geological contexts, including deep saline aquifers (e.g., Sleipner, Quest, Gorgon, Otway) and depleted or producing hydrocarbon reservoirs (e.g., Weyburn, Cranfield), providing a robust benchmark for comparison.

In terms of storage capacity, these projects typically range from several tens to hundreds of millions of tonnes of CO₂. For instance, Sleipner has been injecting approximately 1 MtCO₂ per year since 1996 into a saline aquifer, while Gorgon represents one of the largest projects globally, with planned storage on the order of hundreds of millions of tonnes. Similarly, Quest has stored several million tonnes of CO₂ in a deep saline formation, and Weyburn and Cranfield demonstrate significant storage potential in carbonate and sandstone reservoirs associated with hydrocarbon systems. These sites are characterized by well-constrained structural or stratigraphic traps, adequate reservoir quality (porosity and permeability), and effective sealing formations.

Within this global context, the capacities estimated in the present study fall within a comparable order of magnitude, considering the scale of evaluation and available data. The geological setting, involving sedimentary formations with suitable petrophysical properties and structural configurations, further supports the relevance of the comparison. Although uncertainties remain—particularly related to data density and model resolution—the results suggest that the studied reservoirs share key characteristics with established storage sites.

MODEL UNCERTAINTIES

Effective capacity is typically estimated using probabilistic volumetric approaches that incorporate storage efficiency coefficients derived from numerical simulations and calibrated with petrophysical data. Such methods allow the integration of geological variability and uncertainty, providing a range of possible storage values rather than a single deterministic estimate. Effective capacity thus represents a more realistic and operationally relevant assessment of storage potential and serves as an intermediate metric between theoretical and practical capacities, particularly useful for site screening and early-stage evaluations (CSLF, 2007; USDOE, 2007; Bachu et al., 2007; IEA-GHG, 2009).

A major challenge in estimating effective capacity lies in the quantification of uncertainties, especially those related to seismic interpretation and interpolation of reservoir properties. Seismic data define reservoir geometry and structure but are affected by resolution limits, velocity model uncertainties, and interpretation subjectivity. These uncertainties propagate into key volumetric parameters such as thickness and reservoir extent, and are further amplified during time-to-depth conversion in heterogeneous formations. Similarly, the interpolation of petrophysical properties between wells introduces additional uncertainty. Given these cumulative uncertainties, deterministic values can be misleading. A probabilistic framework is therefore essential, where uncertainty is propagated through volumetric calculations to generate distributions of storage capacity. The use of statistical percentiles (P10, P50, P90) allows the definition of reliable ranges, with P50 representing the most likely value and P10–P90 bounding optimistic and conservative scenarios. Expressing storage capacity as percentile ranges provides a robust and transparent basis for risk-informed decision-making, particularly in early-stage assessments where data limitations are significant.

SUMMARY AND CONCLUSION

The Cahuasa Upper Jurassic formation in the Coyula seismic block shows promising characteristics for CO₂ storage, including permeable strata sealed by impermeable layers at depths suitable for injection (3500-4000m). Identified saline aquifers exhibit high permeability (0.2-6.05 mD for sandstone and clay intercalations) and porosity ranging from 0.07% to 0.2%, making them suitable for CO₂ storage. These layers are suitable reservoir rocks qualified for permanent CO₂

storage. The CO₂ storage potential in the Cahuasas formation at the Coyula block was calculated based on the rock compositions and petrophysical properties from exploratory oil wells. Three stratigraphic reservoirs, called A, B and C were identified sealed by Huehuetepc shale formation. The prospective storage resources of the three reservoirs were calculated locally, integrating seismic profiles and wells data considering the open and close systems hypothesis. In this case the close system will be the most conservative results (16.11 to 25.62 Mton CO₂) as a first site evaluation. This study suggests that the CO₂ storage capacity ranges approximately for open system from 25.65 to 40.78 Mton (lower range), and 75.36 to 119.82 Mton (maximum conditions). Summing the three Cahuasas formation reservoirs, the geological storage efficiencies range from 0.08% to 4.3%. The results obtain from the close system hypothesis are comparable to the lower characteristic ranges (P10) of the open system. The Cahuasas formation within the Coyula block, representing less than 10% of the Tampico Misantla basin, demonstrates significant CO₂ storage potential, exceeding the estimated annual CO₂ emissions from the basin's oil industry (approximately 4 Mton; Medina et al., 2023).

The uncertainty associated with subsurface data gaps was incorporated into the storage resource evaluation due to the legacy of seismic data and the relatively limited well data available over the study area. As well, the upper Jurassic reservoirs show evidence of alluvial fan geometry and natural permeability heterogeneity and/or reactivation structures (Figure 1, Aguayo-Camargo et al., 2018). Jurassic faults and lateral permeability variation are potentially boundaries defining a “semi-closed system” from which the lateral displacement of brine during CO₂ injection might be prevented and contained, avoiding a pressure buildup in the reservoir (e.g., Zhou et al., 2008).

Overall, the comparison with reference sites indicates that the storage potential identified is credible and sufficiently robust to justify advancing to the next stage of detailed evaluation. This should include refined geological and dynamic modeling, improved constraint of petrophysical parameters, and a more comprehensive uncertainty assessment, in order to better define injectivity, containment, and long-term storage performance.

Acknowledgments. This research is part of the first author's PhD project in the framework of the Universidad Nacional Autónoma de México (UNAM) Postgraduate Program. The research was funded by SENER-CONACYT grant CB-263486 to G. Levresse. We are grateful to the Comision

Nacional de Hidrocarburos, and the Secretaria de Energia for the technical support and data access through the ARES-NVR-MX-16-4Y8 agreement.

Declaration of competing interest. The authors declare that they have no known competing financial interests or personal relationships that could have appeared to influence the work reported in this paper.

Funding: CONACYT grant CB-263486

REFERENCES

- Ahmed, A.J. (2006). Compressibility of porous rocks: Part II. New relationships. Petroleum Engineering Department. *Acta Geophysica*, 54(4) 399–412. <https://doi.org/10.2478/s11600-006-0029-4>
- Al-Khoury, R., & Bundschuh, J. (2014) Computational Models for CO₂ Geo-sequestration and Compressed Air Energy Storage. *Taylor & Francis*.
- Aranda-Gómez, J.J., Housh, T.B., Luhr, J.F., Henry, C.D., Becker, T., & Chávez-Cabello, G., (2005). Reactivation of the San Marcos fault during mid- to late Tertiary extension, Chihuahua, México. In J.A. Nourse, T.H., Anderson, J.W., McKee, M.B., Steiner, (eds.), The Mojave-Sonora megashear hypothesis: Development, assessment, and alternatives: *Geological Society of America, Special Paper*, 393, 509–522. <https://doi.org/10.1130/0-8137-2393-0.509>
- Archie, G.E. (1942). The Electrical Resistivity Log as an Aid in Determining Some Reservoir Characteristics. *Transactions of the AIME*, 146, 54–62.
- Barker, R.R.W., & Berggren, W.A. (1977). Paleocene and Early Eocene of the Rio Grande and Tampico Embayments: iferal biostratigraphy and paleoecology. *Marine cropaleontology*, 2, 67–103.
- Bassiouni, Z. (1994). Theory, Measurement and Interpretation of Well Logs Tulsa, Oklahoma, USA. *SPE Textbook Series 4*.
- Bowers, G.L. (1995). Pore pressure estimation from velocity data: accounting for overpressure mechanisms besides under compaction. *SPE Drilling & Completion*, 10, 89–95. doi: <https://doi.org/10.2118/27488-PA>
- Camacho-Angulo, F. (1993), *Compilación geológica de la vertiente del Golfo de México: Veracruz, Ver.* Comisión Federal de Electricidad, Subdirección Técnica, Gerencia de Estudios de Ingeniería Civil, Subgerencia de Estudios Geológicos, Departamento de Geología, Zona Golfo, 169 pp.

- Carrillo-Bravo, J. (1971). La Plataforma de Valles San Luis Potosí. *Boletín de la Asociación Mexicana de Geólogos Petroleros*, 23, 102 pp.
- Coates, G. R., & Dumanoir, J. L. (1973). A new approach to improved log derived permeability. *SPWLA Fourteenth annual logging symposium*, 1–28.
- Coombs, H., Kerr, A., Pindell, J., Buchs, D., Weber, B., Solari, L. (2020). Petrogenesis of the crystalline basement along the western Gulf of Mexico: Post-collisional magmatism during the formation of Pangea. In U. C. Martens, R. S. Molina Garza (Eds.), Southern and Central Mexico: Basement Framework, Tectonic Evolution, and Provenance of Mesozoic–Cenozoic Basins. *GSA Special Papers*, 546, 29–52. [https://doi.org/10.1130/2020.2546\(02\)](https://doi.org/10.1130/2020.2546(02))
- Comisión Nacional de Hidrocarburos (CNH) (2018). *Atlas geológico cuenca tampico-misantla. Versión 3.* Centro Nacional de Información de Hidrocarburos. https://hidrocarburos.gob.mx/media/3091/atlas_geologico_cuenca_tampico-misantla_v3.pdf
- Eaton, B. (1972). The Effect of Overburden Stress on Geopressure Prediction from Well Logs. *Journal of Petroleum Technology*, 24(8), 929–934. SPE-3719-PA. <http://dx.doi.org/10.2118/3719-PA>
- Eaton, B.A. (1975). The Equation for Geopressure Prediction from Well Logs. Fall Meeting of the Society of Petroleum Engineers. *SPE 5544*, october, 1975. <https://doi.org/10.2118/5544-MS>
- Eguiluz de Antuñano, S. (2011). Sinopsis geológica de la Cuenca de Burgos, noreste de México: producción y recursos petroleros. *Boletín de la Sociedad Geológica Mexicana*, 63, 323–332.
- Esquivel-Macías, C., León-Olvera, R.G., & Flores Castro K. (2017). Paleoenvironment and biostratigraphy of the Upper Sinemurian (Lower Jurassic) of the Huayacocotla Formation in East-Central Mexico. *Boletín de la Sociedad Geológica Mexicana*, 69(3), 739–770. <http://dx.doi.org/10.18268/BSGM2017v69n3a12>
- Ferrari, L., Tagami, T., Eguchi, M., Orozco-Esquivel, M. T., Petrone, C., Jacobo-Albarrán, J., & López-Martínez, M. (2005). Geology, geochronology and tectonic setting of late Cenozoic volcanism along the southwestern Gulf of Mexico: the Eastern Alkaline Province revisited. *Journal of Volcanology and Geothermal Research*, 146(4), 284–306. <https://doi.org/10.1016/j.jvolgeores.2005.02.004> rights and content
- Fitz-Díaz, E., Lawton, T. F., Juárez-Arriaga, E., & Chávez-Cabello, G. (2018). The Cretaceous-Paleogene Mexican orogen: Structure, basin development, magmatism and tectonics. In A. Gómez-Tuena, F. Ortega-Gutiérrez (Eds.), Tectonic Systems of Mexico: Origin and Evolution. *Earth-Science Reviews*, 183, 56–84. <https://doi.org/10.1016/j.earscirev.2017.03.002>

- Guzmán-Arellano, G. J. (2012). *Evaluación petrolera y método de explotación de la región Tampico Misantla* [Bachelor Thesis]. Facultad de Ingeniería, Universidad Nacional Autónoma de México.
- Hamblock, J. M. (2002). *Lithology, mineralization and alteration in the Eastern Alkaline Province* [M. Sc. Thesis]. Universidad de Arizona.
- Hatzignatiou, D.G., Riis, F., Berenblyum, R., Hladik, V., Lajka, R., & Francu, J. (2011). Screening and evaluation of a saline aquifer for CO₂ storage: Central Bohemian Basin, Czech Republic. *International Journal of Greenhouse gas Control*, 5, 1429-1442. <https://doi.org/10.1016/j.ijggc.2011.07.013>
- Hernández-Mendoza, J. J., Escamilla-Hernández, A., De la Huerta-Cobos, M. L., Saavedra-Torres, D. (2011). Depositional Systems in the Chicontepec Basin, Central-Eastern Gulf Coast, Mexico. *Gulf Coast Association of Geological Societies Transactions, 61 Annual Convention*.
- Hernández-Romano, U., Aguilera-Franco, N., Martínez-Medrano, M., Barceló-Duarte, J. (1997). Guerrero-Morelos Platform drowning at the Cenomanian–Turonian boundary, Huitziltepec area, Guerrero State, southern México. *Cretaceous Research*, 18(5), 661–686. <https://doi.org/10.1006/cres.1997.0078>
- IEA-GHG (2009). *Development of storage coefficients for CO₂ storage in deep saline formations* (Technical study report 2009/13). IEA Greenhouse Gas R&D Programme.
- Lawton, T. F., Juárez-Arriaga, E., Ocampo-Díaz, Y. Z. E., Beltrán-Triviño, A., Martens, U., & Stockli, D. (2016). Evolution of late Cretaceous-Paleogene foreland sediment-dispersal systems of Northern and Central Mexico. *35th Annual GCSSEPM, Foundation Perkins-Rosen Research Conference Programs and Abstracts, Houston, Texas*, 216–233.
- López-Doncel, J. (2003) La Formación Tamabra del Cretácico medio en la porción central del margen occidental de la Plataforma Valles-San Luis Potosí, centro-noreste de México. *Revista Mexicana de Ciencias Geológicas*, 20(1), 1–19.
- López-Infanzón, M. (1986). Estudio petrogenico de las rocas ígneas en las formaciones Huizachal y Nazas. *Boletín de la Sociedad Geologica Mexicana*, 47(2), 1–37.
- Luo, A., Yongming, L., Chen, X., Zhu, Z., & Peng, Y. (2022). Review of CO₂ sequestration mechanism in saline aquifers. *Natural Gas Industry*, 9, 383–393. <https://doi.org/10.1016/j.ngib.2022.07.002>
- Martini, M. & Ortega, F. (2018). Tectono-stratigraphic evolution of eastern Mexico during the break-up of Pangea: A review. *Earth-Science Reviews*, 183, 38–55. DOI: 10.1016/j.earscirev.2016.06.013

- Matthews, W.R. & Kelly J. (1967). How to predict formation pressure and fracture gradient. *Oil and Gas Journal*, 65, 92–1066.
- Medina, E., Levresse, G., Carrera, J., & Cerca, M. (2023). A basin scale assessment framework of onshore aquifer-based CO₂ suitability storage in Tampico Misantla basin, Mexico. *International Journal of Greenhouse Gas Control*, 125, 103874, DOI: <https://doi.org/10.1016/j.ijggc.2023.103874>
- Nava-Perez, M., & Alegria-Luna, M.A. (2001). Los sistemas petroleros de la región de Tampico-Misantla [Bachelor Thesis]. Facultad de Ingeniería, Universidad Nacional Autónoma de México.
- Poliquin, M. J. (2009). *Geology, Geochemistry and age of intrusion-related mineralisation in eastern Mexico* [Ph. D. Thesis]. Exter University.
- Pindell, J., Villagómez, D., Molina-Garza, R., Graham, R., & Weber, B. (2020). A revised synthesis of the rift and drift history of the Gulf of Mexico and surrounding regions in the light of improved age dating of the Middle Jurassic salt. *Geological Society, London, Special Publications*, 504, 29–76. <https://doi.org/10.1144/SP504-2020-43>
- Rodríguez–Hernández, E., Lopez Doncel, R., Barboza Gudiño, J.R., & Cruz Marquez, J. (2007). Análisis sedimentológico-facial de clastos formadores de brechas calcáreas cretácicas de una zona transicional plataforma–cuenca en el centro de México. *Revista Mexicana de Ciencias Geológicas*, 26, 687–708.
- Roure, F., Alzaga-Ruiz, H., Callot, J.P., Ferket, H., Granjeon, D., Gonzalez-Mercado, G.E., Guilhaumou, N., Lopez, M., Mougín, P., Ortuno-Arzate, S., Séranne, M. (2009). Long lasting interactions between tectonic loading, unroofing, post-rift thermal subsidence and sedimentary transfers along the western margin of the Gulf of Mexico: Some insights from integrated quantitative studies. *Tectonophysics*, 475(1), 169–189. <https://doi.org/10.1016/j.tecto.2009.04.012>
- Santillán-Piña, N., & Aguayo-Camargo, J. E. (2011). Lower Tertiary Sedimentary Turbidite Facies at the Chicotepec Basin, East-Central Mexico. *Ingeniería Investigación y Tecnología*, XII(3), 337–352
- Seegerstrom, K. (1962). Geology of South-central Hidalgo and Northeastern México, Mexico. *United States Geological Survey Bulletin*, 1104-C, 87–162.
- Seibertz, E. (1986). Paleogeography of the San Felipe Formation (Mid-Cretaceous, NE Mexico) and facial effects upon inoceramids of the Turonian/Coniacian transition. *Zentralblatt für Geologie und Paläontologie*, I(9/10), 1171–118. DOI: 10.1127/zbl_geol_pal_1/1985/1986/1171
- Servicio Geológico Mexicano (1997). Carta geológica-minera Ciudad Valle, F14-8, 1:250 000.

- Servicio Geológico Mexicano (1997). Carta geológica-minera Pachuca, F14-11, 1:250 000.
- Servicio Geológico Mexicano (1999). Carta geológica-minera Ciudad Mande, F14-5, 1:250 000.
- Servicio Geológico Mexicano (2002). Carta geológica-minera Veracruz, E14-3, 1:250 000.
- Servicio Geológico Mexicano (2004). *Carta geológica-minera Ciudad Victoria, F14-2, 1:250 000.*
- Servicio Geológico Mexicano (2004). Carta geológica-minera Poza Rica, F14-12, 1:250 000.
- Servicio Geológico Mexicano (2004). Carta geológica-minera Tampico, F14-3-6, 1:250 000.
- Servicio Geológico Mexicano (2004). Carta geológica-minera Tamiahua, F14-9, 1:250 000.
- Suter, M. (1980). Tectonics of the external part of the Sierra Madre Oriental foreland thrust-and-fold belt between Xilitla and the Moctezuma River (Hidalgo and San Luis Potosi states). *Revista del Instituto de Geología, Universidad Nacional Autónoma de México, 4*, 19–31.
- Todd, R.G. (1976). Oolite-Bar Progradation, San Andres Formation, Midland Basin, Texas. *AAPG Bulletin, 60*(6), 907–925. <https://doi.org/10.1306/C1EA35DC-16C9-11D7-8645000102C1865D>
- Torp, T.A., & Gale J. (2003) Demonstrating storage of CO₂ in geological reservoirs, the Sleipner and SACS projects. *Proceedings of the 6th International Conference on Greenhouse Gas Control Technologies. Kyoto, Japón*, V1- 311–316.
- Viera-Décida, F., Ramirez Fernandez, J.A., Velasco Tapia, F., & Orozco Esquivel, M.T. (2009). Relaciones petrogenéticas del magmatismo en la provincia Alcalina Oriental mexicana. *Ciencias UANL, 12*(1), 42–49.
- Wyllie, M.R.J., & Rose, W.D. (1950). Some Theoretical Considerations Related to the Quantitative Evaluation of the Physical Characteristics of Reservoir Rock from Electric Log Data. *Transaction of American Institute of Mining Engineers, 189*, 105–118.
- Zhou, Q., Bitkholzer, J.T., Tsang, C.F., Rutqvist, J. (2008). A method for quick assessment of CO₂ storage capacity in closed and semi-closed saline formations. *International Journal of Greenhouse Gas Control, 2*, 626–639.
- Zimmerman, R.W. (1991). *Compressibility of sandstones. Development in Petroleum Science*. Elsevier Science Publishers, vol. 29.

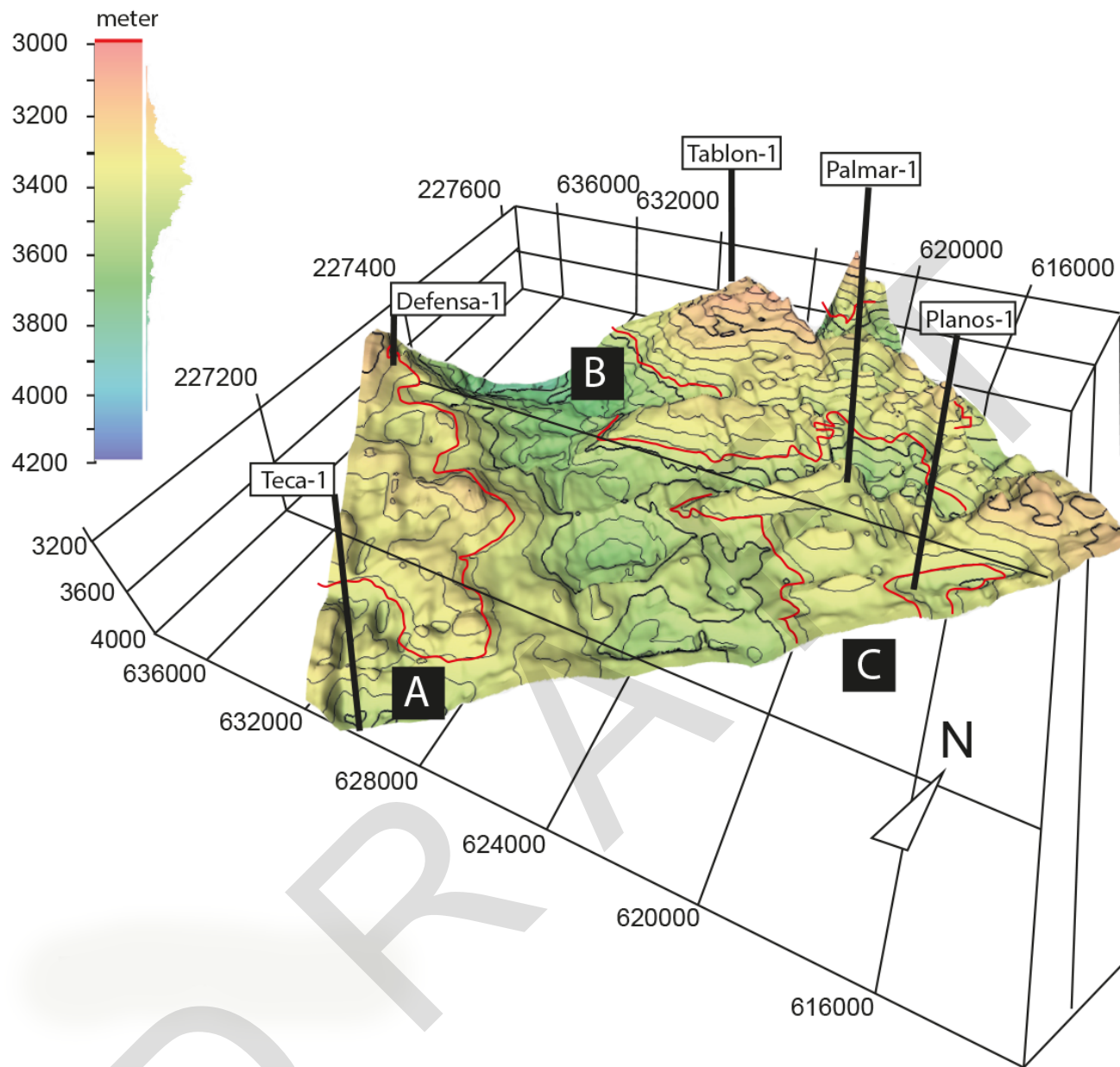


Figure 2. Location of the wells Planos-1, Tablon-1, Tecomate-1 (Teca-1), Palmar-1, Defensa-1, at the top of the Cahuassas Upper Jurassic formation.

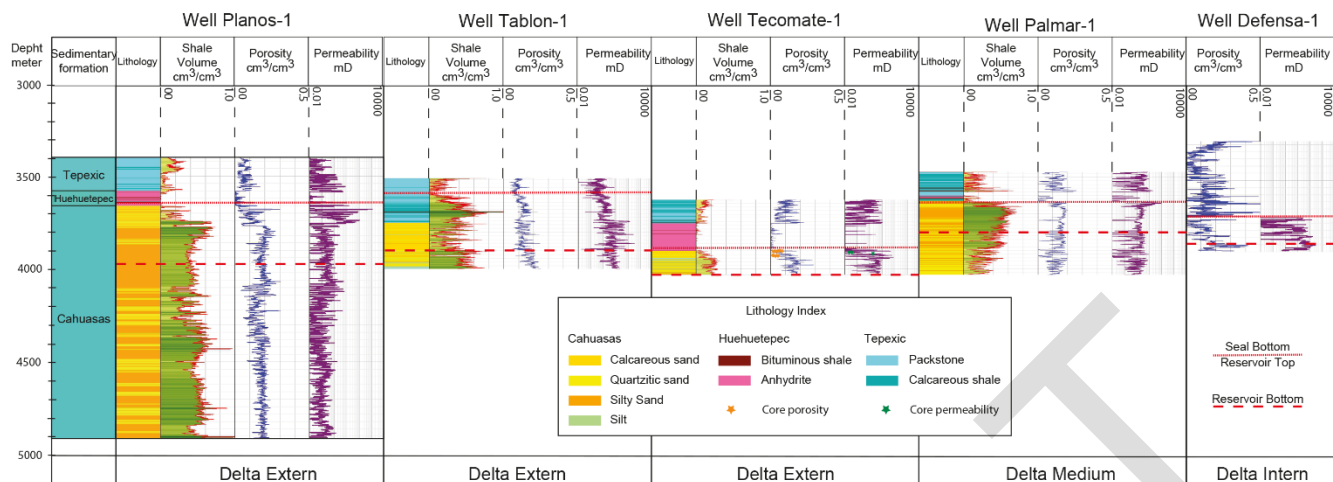


Figure 3. Stratigraphic, lithology and petrophysics correlation of the Jurassic sequences from the wells Planos-1, Tablon-1, Tecamate-1 (Teca-1), Palmar-1, Defensa-1.

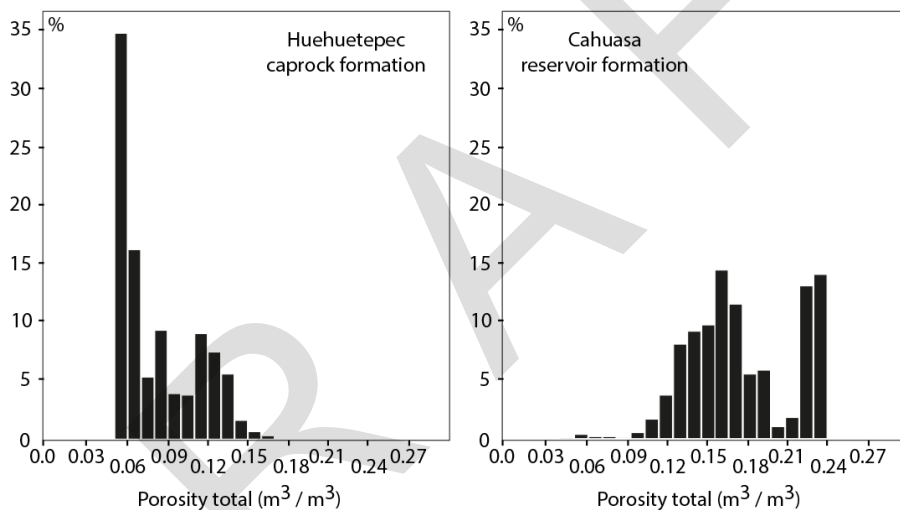


Figure 4. Porosity values distribution of the upper part of the Cahuasa reservoir section and the Huehueteppec caprock formations from the Tecamate-1 well petrophysics and samples laboratory analysis.

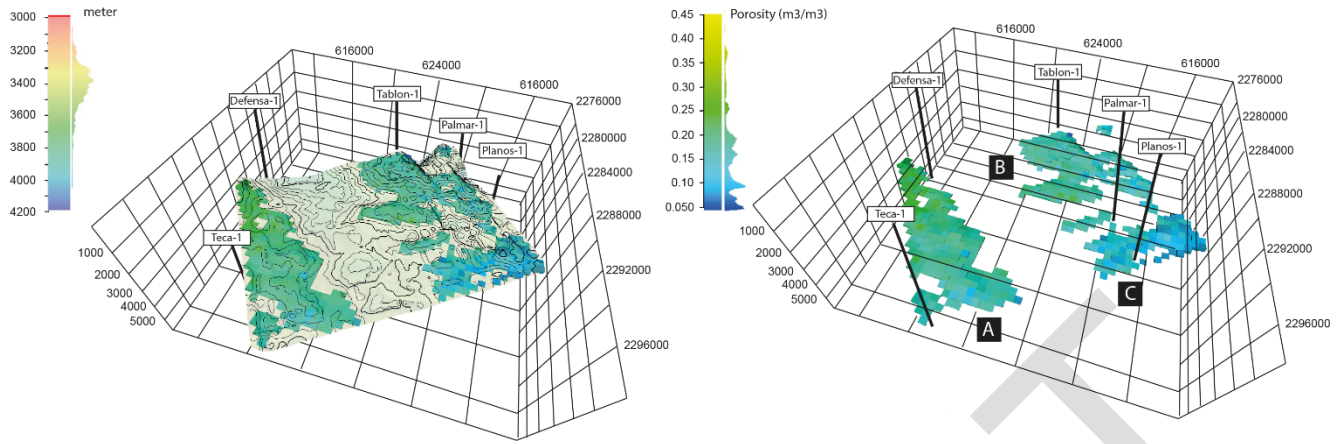


Figure 5. Stratigraphic, lithology and petrophysics correlation of the Cahuasas Jurassic formation. (A) surface of the top of the Cahuasas Jurassic formation. (B) Porosity 3D block variation. The red line delimits the bottom of the reservoirs A, B and C.

DRAFT

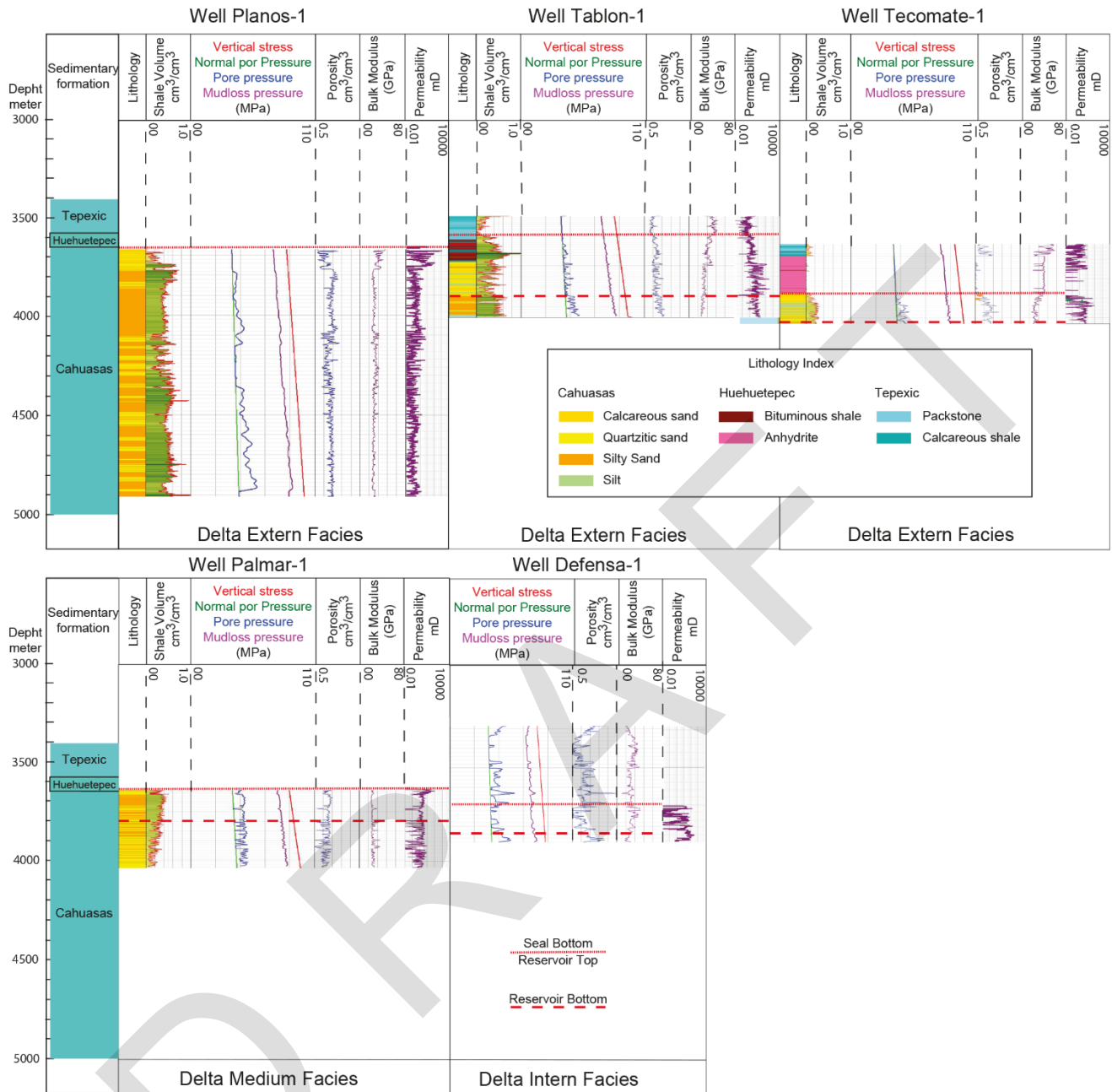


Figure 6. Stratigraphic, lithology and calculated petrophysics properties (wells and laboratory) of the Jurassic sequences from the wells Planos-1, Tablon-1, Tecamate-1, Palmar-1, Defensa-1,

TABLES

Table 1. Synthesis of petrophysics characteristics determined for each stratigraphy level for the different reservoirs (A, B, C).

	Well	depth (m)	Overpressure	Pore Pressure	Fracture Pressure	Compressibility mode	Porosity	Permeability
			(MPa)	(MPa)	(MPa)	(K)	(m ³ /m ³)	(mD)
Reservoir - A	Tecoman-101	3900-3940	92.6	39.9	87.6	26.6	0.08	0.26
	Tecoman-101	3950-4025	94.5	40.7	90.8	26.2	0.16	2.4
	Defensa-101	3600-3650	84.1	36.9	72.8	24.2	0.07	0.52
	Defensa-101	3665-3690	85.4	47.2	76.4	22.4	0.2	2.5
Reservoir - B	Planos-1	3580-3620	86.2	36.9	75.8	36.3	0.08	0.6
	Planos-1	3800-3900	91.9	42.1	80.9	27.9	0.14	0.02
	Planos-1	4000-4050	96.1	49.0	85.1	22.6	0.17	0.13
Reservoir - C	Tablón-1	3730-3760	89.2	41.7	77.7	26.9	0.13	6.05
	Tablón-1	3790-3890	91.2	39.1	76.7	27.4	0.12	5.99
	Tablón-1	3930-3990	94.8	47.1	83.4	23.6	0.18	5.47
	Palmar-1	3630-3660	88.1	40.8	76.8	23.9	0.11	5.82
	Palmar-1	3800-3850	92.3	49.5	82.3	21.1	0.13	0.82
	Palmar-1	3950-4000	95.8	48.0	84.7	23.2	0.14	1.05
	K (Pa)	β_r (1/K)(Pa-1)	β_a (Pa-1)	Pf (Pa)	Pp (Pa)	ΔP (Pa)	$\beta_a + \beta_r$ (Pa-1)	Ecomp
Reservoir - A	26593000000	3.76039E-11	4.6E-10	87563000	39918000	47645000	4.97604E-10	0.024
	26163000000	3.82219E-11	4.6E-10	90785000	40726000	50059000	4.98222E-10	0.025
	24213000000	4.13001E-11	4.6E-10	72839000	36851000	35988000	5.013E-10	0.018
	22420000000	4.4603E-11	4.6E-10	76370000	47169000	29201000	5.04603E-10	0.015
Reservoir - B	36254600000	2.75827E-11	4.6E-10	75759000	36895300	38863700	4.87583E-10	0.019
	27948000000	3.57807E-11	4.6E-10	80949000	42114000	38835000	4.95781E-10	0.019
	22571000000	4.43046E-11	4.6E-10	85092000	48973000	36119000	5.04305E-10	0.018
Reservoir - C	26872000000	3.72135E-11	4.6E-10	77651000	41659000	35992000	4.97213E-10	0.018
	27430000000	3.64564E-11	4.6E-10	76682000	39076000	37606000	4.96456E-10	0.019
	23613000000	4.23496E-11	4.6E-10	83396000	47136000	36260000	5.0235E-10	0.018
	23930100000	4.17884E-11	4.6E-10	76846000	40843200	36002800	5.01788E-10	0.018
	21085000000	4.74271E-11	4.6E-10	82262000	49463000	32799000	5.07427E-10	0.017
	23186000000	4.31295E-11	4.6E-10	84736000	48046000	36690000	5.03129E-10	0.018

Table 2. CO₂ storage potential for the Coyula Block, for a close system hypothesis. Results are presented by reservoirs (A, B, C).

Close system	V (MOVE) m3	φ (AVERAGE)	CO ₂ DENSITY		E _{comp} AVERAGE	Effective storage capacity. Volume m3 (Vφ*E) AVERAGE	Effective storage capacity, Mass Mtoe (Vφ*E*ρ)	
			MIN	MAX			MIN	MAX
Reservoir - A	3549127186	12.75	417	663	2.03	9186028.439	3.83	6.09
Reservoir - B	4832742533	13			1.88	11811222.75	4.93	7.83
Reservoir - C	7300852499	13.50			1.79	17642510.06	7.36	11.70
Total							16.11	25.62

Table 3. Petrophysical estimation for the Coyula Block, for an open system hypothesis. Results are presented by reservoirs (A, B, C).

Close system	V (MOVE) m3	φ (AVERAGE)	CO ₂ DENSITY		E _{comp} AVERAGE	Effective storage capacity. Volume m3 (Vφ*E) AVERAGE	Effective storage capacity, Mass Mtoe (Vφ*E*ρ)	
			MIN	MAX			MIN	MAX
Reservoir - A	3549127186	12.75	417	663	2.03	9186028.439	3.83	6.09
Reservoir - B	4832742533	13			1.88	11811222.75	4.93	7.83
Reservoir - C	7300852499	13.50			1.79	17642510.06	7.36	11.70
Total							16.11	25.62

Table 4. CO₂ storage potential for the Coyula Block, for an open system hypothesis. Results are presented by reservoirs (A, B, C).

ID	V (MOVE) m3	φ	DENSITY CO ₂		Ee (%)			Effective storage capacity. Volume m3 (Vφ*E)			Effective storage capacity. Mass Mtoe (Vφ*E*ρ)					
			MIN	MAX	P10	P50	P90	min	50	max	min		50		máx.	
											417	663	417	663	417	663
Reservoir - A	3549127186	12.75	417	663	5.94	9.4	14.48	26879314.7	42536289.32	65523986.11	11.21	17.82	17.74	28.20	27.32	43.44
Reservoir - B	4832742533	13			1.48	2.04	3.7	9298196.63	12816433.2	23245491.58	3.88	6.16	5.34	8.50	9.69	15.41
Reservoir - C	7300852499	13.5			2.57	3.71	9.33	25330307.7	36566319.74	91957887.65	10.56	16.79	15.25	24.24	38.35	60.97
Total											25.65	40.78	38.33	60.94	75.36	119.82